

# CMOS-Compatible, Flexible, Intracortical Neural Probes

Falk Barz<sup>1</sup>, Vanessa Trouillet, Oliver Paul<sup>1</sup>, Member, IEEE, and Patrick Ruther<sup>1</sup>, Member, IEEE

**Abstract**—Flexible intracortical neural probes elicit a lower foreign body response when compared to rigid implants. However, by incorporating complementary metal-oxide-semiconductor (CMOS) circuitry, silicon-based neural probes can offer an improved scalability and more functionalities than any other currently available technology. **Objective:** Our goal is the development of a novel neural probe that combines flexibility with the functionalities of active CMOS-based probes. **Methods:** We interface CMOS-based probe tips of only a few millimeters in length with flexible polyimide cables, which enable the complete implantation of the tips into brain tissue. The multilayer platinum metallization of the cables is patterned using a novel combination of ion beam and plasma etching. Implantation of the flexible probes is verified in brain models using stiff insertion shuttles. **Result:** We assembled neural probes from passive and active tips as short as 1.5 mm and less than 180  $\mu\text{m}$  in width. Active probes feature electrode arrays with 72 recording sites and multiplexing to 16 parallel output lines. We reliably patterned cables with signal lines of 2  $\mu\text{m}$  in width and 3  $\mu\text{m}$  in spacing. Ion beam etching deteriorated the composition of the polyimide substrate and its resistance to around 1 k $\Omega$ . An additional plasma treatment re-established high insulation resistances and recovered the chemical composition. Probes were successfully implanted to a depth of 7 mm using insertion shuttles and withstood forces of 63 mN. **Conclusions:** This study presents the methods required for the fabrication and application of a new generation of neural probes. **Significance:** The synergistic approach surpasses the limitation of each individual probe technology and should be considered in future developments.

**Index Terms**—Flexible neural probe, CMOS, polyimide, ion beam, oxygen plasma materials processing, XPS, probe insertion methods.

Manuscript received May 2, 2019; revised July 19, 2019; accepted August 12, 2019. Date of publication August 21, 2019; date of current version April 21, 2020. This work was supported by the project EUJO-LIMMS (295089) funded by the EU 7th Framework Program and the Cluster of Excellence BrainLinks-BrainTools funded by German Research Foundation (DFG) under Grant EXC 1086. The K-Alpha+ instrument was supported by the German Federal Ministry for Economic Affairs and Energy (BMWi) under Grant 03ET6040 on the basis of a decision by the German Bundestag. (*Corresponding author:* Falk Barz.)

F. Barz is with the Department of Microsystems Engineering (IMTEK), University of Freiburg, Freiburg im Breisgau 79085, Germany (e-mail: falk.barz@imtek.de).

V. Trouillet is with the Karlsruhe Nano Micro Facility and Institute for Applied Materials, Karlsruhe Institute of Technology.

O. Paul and P. Ruther are with the Department of Microsystems Engineering (IMTEK), University of Freiburg, and also with the Cluster of Excellence BrainLinks-BrainTools, University of Freiburg.

Digital Object Identifier 10.1109/TBME.2019.2936740

## I. INTRODUCTION

RECENT developments of intracortical neural probes aim for an improved biocompatibility, but also for large-scale neural recording capability of the implant. Passive, flexible neural probes composed of polymer substrates, like polyimide (PI) or parylene-C, and thin-film metallizations are often proposed as an attempt to meet both requirements [1]. The reduced mechanical stiffness of these substrates compared to other commonly used materials, such as metals or silicon (Si), can improve the acceptance of the probe by the host tissue [2]. Yet, most of these passive polymer-based devices do not meet the channel count or channel density of their rigid counter parts. Indeed, all high channel count systems (simultaneously recorded neurons >100) identified by Stevenson and Kording in their review on large-scale neural recoding systems are rigid and have been either assembled from microwires or fabricated from Si using microelectromechanical systems (MEMS) processes [3]. Especially with the advent of active Si-based neural probes that incorporate microelectronic IC for signal conditioning and multiplexing [4], significantly larger numbers of recording sites have been implemented in a single neural probe than with any other technological approach [5]. Furthermore, smaller implant dimensions can be realized by multiplexing recording sites to a reduced number of output channels and the generally higher patterning resolution offered by CMOS processes. As the device dimensions are critical in view of the biocompatibility of an implant [6], [7], active probes with geometric properties untied from their channel count, gain a considerable advantage over passive, large-scale recording systems. For passive systems, the wiring of the recording sites will inevitably become the main bottleneck when scaling up the channel count.

The common implementation of active probes exhibits, however, a lower biocompatibility than polymer-based implants. This is in part caused by the stiffness of the Si substrate, but also due to the probe design featuring one or several slender penetrating shanks rigidly connected to a larger probe base. This base serves as an interface for transferring the wiring of the recording sites on the probe shank to the external recording or stimulation instrumentation. In extreme cases, probe bases are larger than 1 cm<sup>2</sup> [5]. Even in very compact approaches [8], the base is normally too large for sub-dural placement or implantation into cortical tissue. Consequently, for chronic recordings, the base has to reside above the brain where it is rigidly or flexibly connected to the skull. This setup, in addition, requires that the rigid probe shanks penetrate through the brain meninges into

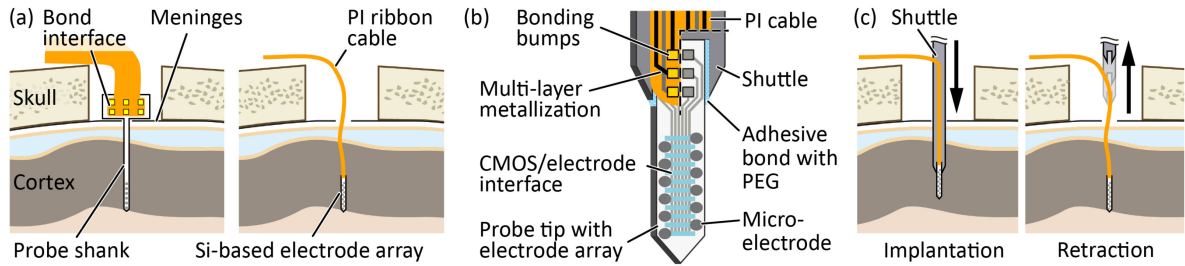


**Fig. 1.** Schematic representation of (a) conventional Michigan-style and novel hybrid silicon-polymer neural probe. (b) Detailed view of the tip of the ultra-compact active probe. (c) Probe implantation and shuttle retraction.

the brain tissue. The tethering of the base and the contact point of the shanks with the dura transfer forces to the rigid probe that originate from the relative motion between skull and brain. These forces will result in probe displacement and mechanical stress in the brain tissue. The stimulus on the tissue elicits an increased foreign body response (FBR) and ultimately degrades the quality of the neural recording [2].

The mechanical stress exerted on the tissue can be alleviated by minimizing the motion-related forces acting on the implanted section of the probe. This is the case for polymer-based neural probes whose flexibility attenuates the amplitude of the reaction forces in the tissue. However, even rigid implants made from metals or Si will impose less mechanical stress on the brain and elicit a drastically lowered FBR when the tethering forces are avoided or strongly reduced [7], [9]. A practical solution to reduce the tethering forces acting on a rigid implant has recently been presented for a passive Si-based probe [10]. The design features a single, rigid probe shank with miniaturized interface that is implanted flush with the surface of the cortex and tethered to the skull only by a flexible PI cable. Relative motion between brain and skull should result in similar forces for this probe compared to an implant made entirely from polymer, but the stress in the tissue should still be higher due to the complete rigidity of the implanted portion of the probe [11]. Previously, we presented a passive, Si-based neural probe featuring an even more progressive design that substitutes large portions of the implanted section by PI to increase its compliance and further reduce the mechanical stress in the tissue [12]. Implementing CMOS IC on the Si-based section of such an implant would result in an ultra-compact, active neural probe that floats in the brain tissue avoiding the major geometrical and mechanical disadvantages of commonly applied active systems.

In this work, we present an active neural probe where the Si substrate required for CMOS integration is reduced to the bare minimum and constitutes only the tip of the probe. The majority of the probe is made from PI and thus rendered highly flexible. The integrated circuitry allows for multiplexing, which results in a highly compact device. Furthermore, our active probe takes advantage of electronic-depth-control (EDC) to increase the recording robustness of the system. This technique enables the electronic relocation of the recording sites in-situ based on recording quality [13].

In the following, we will first introduce the concept of the hybrid Si-polymer neural probe and the fabrication and assembly of its components. For the realization of the compact

architecture of our probe, we developed an efficient patterning process with high resolution for the signal lines in our polymer cables. A detailed characterization of this process is presented in this work. Finally, we demonstrate the implantation of the flexible probes into brain models composed on agar-gel and polyethylene membranes using stiff insertion shuttles.

## II. MATERIALS AND METHODS

### A. Design of the Hybrid Silicon-Polymer Neural Probe

Fig. 1 compares a conventional Michigan-style neural probe to our concept of a CMOS-compatible, hybrid Si-polymer neural probe. The Michigan-style probe exhibits the commonly employed design with a large interface that connects the Si-based electrode array to a  $\mu\text{m}$ -thin and flexible, but wide ribbon cable {Fig. 1(a), left}. The interface between both probe components is significantly larger than the implanted portion and has to reside outside of the brain. Our hybrid probe concept is characterized by a significant reduction in size of the bond interface {Fig. 1(a&b)}, i.e., cable and probe base have the same, strongly reduced width. This allows to deeply implant the miniaturized Si-based electrode array at the probe tip and replace the rigid probe shank to a large extent by a slender, flexible PI cable.

In the case of CMOS-based probe variants, we implemented on-chip multiplexing of 72 recording sites to 16 parallel analog output lines in the active probe tip. The respective electronics integrated in the stiff probe part has already been presented in detail for the conventional probe design [8]. The applied probe technology combining CMOS and MEMS technologies first introduced in [13] results in an ultra-compact probe tip that is only  $100 \mu\text{m}$  wide and  $3.1 \text{ mm}$  long. We also implemented passive probe tips with 16- or 32-channels and a width of 120 and  $180 \mu\text{m}$ , respectively. The length of these tips lies between 1.5 and 3 mm and mostly depends on the layout of the respective microelectrode array. The thickness of the probe tips is  $50 \mu\text{m}$ . The applied fabrication technology and hybrid assembly approach of our silicon-polymer probes offer highest CMOS compatibility. This compatibility is not only given from a technical point of view, but also economically meaningful as the entire area of the Si substrates can be exploited to realize slender probe tips. This represents a clear advantage over wafer-level fabrication approaches, as detailed in [10], where the Si and polymer components are fabricated on the same wafer and a large portion of the CMOS chip area would be covered by the cables and, thus, lost.

The hybrid assembly concept, however, also creates a bottleneck at the interface region between the two components. Signal lines have to be routed around the bonding pads and bonding bumps in tip and cable, respectively, as indicated in Fig. 1(b). A compact architecture of the complete probe is possible only with multiple metallization layers and small widths and spacings of these signal lines. The lines in the passive probe tips are formed by metal evaporation and lift-off techniques with widths and separations of 2 and 3  $\mu\text{m}$ , respectively. For the PI cables, the realization of similar feature sizes with our established material and process combination, i.e., sputter-deposited platinum (Pt) metallization layers and a lift-off technique, is, admittedly, highly prone to failures. As the material combination of PI and Pt and the sputter deposition method performed reliably for our implantable probes, we chose to implement an ion beam etching processes for line patterning instead of the lift-off process. Details on the process parameters, a characterization of process-related changes of the polymer substrate and the development of a process sequence that eliminates these changes are presented in the following sections.

For probe implantation, we implemented stiff insertion shuttles that precisely fit the distal end of the probe tip in footprint and thickness {Fig. 1(b&c)}. The design of the shuttle guarantees that the track formed by the probe during implantation is only slightly larger than the probe tip alone. Furthermore, the design mitigates additional damage to the cortical tissue at the proximal end of the probe where the electrodes are located. For safe probe implantation, probe and shuttle are temporarily bonded with a small amount of polyethylene glycol {Fig. 1(b)}. Details on the mounting procedure for the shuttle and on the setup for probe insertion into brain phantoms are presented in Section II.D.

### B. Neural Probe Fabrication and Assembly

The passive silicon-based electrode arrays are fabricated on 4-inch silicon substrates using an established probe technology [14]. In short, the fabrication process involves the deposition of stress compensated Si oxide and Si nitride layer stacks by plasma enhanced chemical vapor deposition to form the substrate, intermediate, and top-level insulation layers. Vias between the layers are etched using reactive ion etching (RIE) and photoresist etch masks prior to the deposition of the metallization layers. The wiring is composed of evaporated Au and Pt layers combined with Ti thin films, which we pattern in a lift-off process. The arrays of protruding electrodes are composed of iridium oxide ( $\text{IrO}_x$ ) or Pt with diameters of 15 or 25  $\mu\text{m}$  added by sputter deposition and patterned by lift-off. Using the *etching before grinding* (EBG) technique in the final process step [14], the wafers are thinned down to 50  $\mu\text{m}$  and the chips are released from the substrate. The active, CMOS-based electrode arrays are implemented in a commercial 0.18  $\mu\text{m}$  six-metal, double-poly CMOS process (X-FAB Semiconductor Foundries AG, Erfurt, Germany). Design and fabrication have been reported in detail elsewhere [8], [13]. The post-CMOS process follows the same scheme as used for the passive electrode arrays.

The key technology in our PI cable fabrication is the patterning process for the signal lines using argon ion beam etching (IBE) in combination with a high-resolution positive photoresist etch mask. Previously, sputter deposition and lift-off of the Pt-based metallization layers were used to achieve a resolution of 4 and 6  $\mu\text{m}$  for width and spacing of the signal lines, respectively [15]. The realization of smaller feature sizes for our novel probe design using the established lift-off technology resulted in discontinuous or short-circuited signal lines. These problems are due to defects in the photoresist mask used for lift-off, which we attribute to the thermal budget of the sputtering process and the resulting mechanical deformation of the lift-off mask or a mechanical damage of the metallization during lift-off itself. Furthermore, the process duration was comparably long due to a pulsed Pt sputtering to maintain low substrate temperatures. In addition, the lift-off process requires extended soaking periods in different solvents for complete mask removal. In the process presented here, we decouple the deposition and patterning steps of the metallization. Thereby, we avoid the thermal impact of sputtering on the pattern transfer, and achieve a higher lateral resolution and a lower process duration.

Fig. 2 outlines the complete PI cable fabrication process. As previously reported [15], the process starts with spin-coating of the PI precursor (U-Varnish S, UBE Industries Ltd., Tokyo, Japan) on 4-inch silicon wafers at 3000 rpm {Fig. 2(a)}. After imidization at 450 °C, a 5.5- $\mu\text{m}$ -thick PI layer is obtained. For the first metallization layer, a 250-nm-thin Pt layer is deposited by 13.56 MHz radio-frequency (RF) sputtering at a forward power of 300 W. Next, a 1.8- $\mu\text{m}$ -thick layer of positive photoresist (AZ1518, MicroChemicals GmbH, Ulm, Germany) is patterned as the etch mask using UV photolithography {Fig. 2(b)}. The Pt layer is then etched in a 6-inch broad ion beam source (Nordiko 3000, Hampshire, UK) for 21 min. Ion energy, current density, process pressure, and substrate angle for the ion beam etching (IBE) are 300 eV, 0.8 mA/cm<sup>2</sup>, 0.23  $\mu\text{bar}$ , and 70°, respectively. The parameters result in an etch rate of around 22 nm/min for Pt. As the electrical resistance of the PI surface is significantly reduced after IBE, the wafers are subsequently exposed to an oxygen plasma in a 2.45-GHz plasma etcher (Tetra-30-LF-PC, Diener electronic GmbH + Co. KG, Ebhausen, Germany). The plasma etching (PE) step removes the superficial, ion irradiated PI layer of around 100 nm thickness. Process duration, power, and process pressure are 7.5 min, 750 W, and around 5 mbar, respectively {Fig. 2(c)}. The characterization of the patterning process is detailed in Section II.C. After resist stripping, a 1.9- $\mu\text{m}$ -thick, intermediate PI layer is spin-coated at 10000 rpm. RIE is used to open vias for the subsequent interconnection to the second metallization layer {Fig. 2(d)}. The layer is composed of Pt and tungsten-titanium (WTi) with thicknesses of 200 and 30 nm, respectively. The patterning process employs the same parameters as used for the first metallization layer {Fig. 2(e)}. A final 5.5- $\mu\text{m}$ -thick PI layer is deposited, masked with AZ9260 (MicroChemicals GmbH, Ulm, Germany) and subsequently patterned by RIE to implement the cable contour and bonding pads {Fig. 2(f)}. The WTi layer, which mainly acts as a protective layer for the underlying Pt during RIE, is removed on the pads using H<sub>2</sub>O<sub>2</sub>.

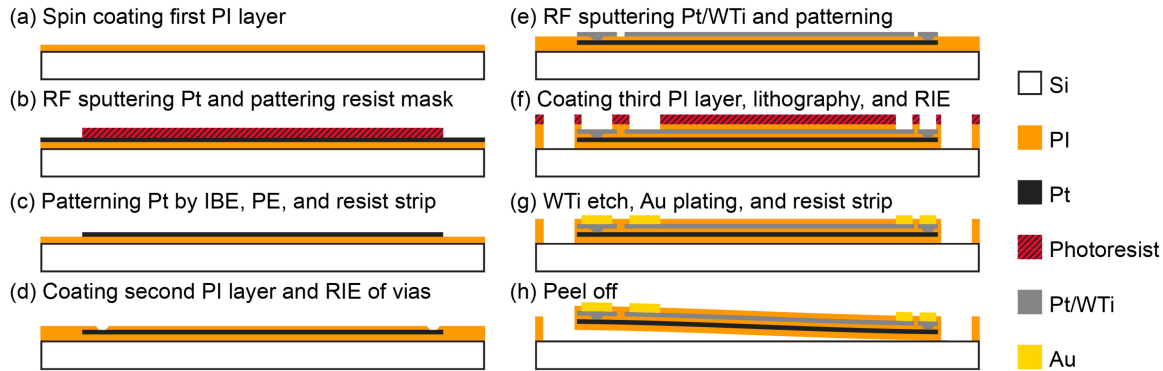


**Fig. 2.** Schematic of fabrication process for the PI cables.

in preparation of the electroplating of the 9- $\mu\text{m}$ -thick bonding bumps {Fig. 2(g)}. After resist stripping and rinsing in deionized water, the individual cables are manually peeled off the wafer using tweezers {Fig. 2(h)}.

In the final probe assembly, the probe tips and cables are bonded using ultrasonic flip-chip (FC) bonding [16]. A commercially available FC bonder with hotplate and ultrasonic module (Fineplacer 96 $\lambda$ , Finetech, Berlin, Germany) was equipped for this purpose with custom-designed microstructured interposer chips to facilitate vacuum gripping of the miniaturized components [12]. Hotplate temperature, total bonding time, US power, and pulse duration are 180 °C, 60 s, 400 mW, and 2 s, respectively. The bonding force was adapted according to the channel count of the probes between 4 and 5 N. Next, the bond interface between the two components is mechanically reinforced and electrically insulated using a biocompatible low-viscosity epoxy underfill (EPO-TEK 301, Epoxy Technology Inc., Billerica, MA, USA). Lastly, the distal end of each probe is soldered to a flexible printed circuit board (PCB).

### C. Characterization of Metal Patterning on PI Substrates

In initial experiments, we found that metallized PI films patterned only by IBE exhibited unacceptably low sheet resistances of the polymer substrate. In extreme cases, the resistance of the insulation between the signal lines was reduced to the k $\Omega$ -range. For the implementation of a reliable patterning process, we deemed it necessary to identify the origin of this change and find suitable countermeasures. A straightforward explanation for the deterioration of the insulation resistance is the prevalence of metal residues on or close to the substrate surface. However, based on the findings of several groups that have studied the effect of Ar ion beam interaction with PI substrates, a second plausible cause is the radiation-induced deterioration of the substrate itself [17]–[20].

Generally, the exposure of PI to an Ar ion beam leads to a change in the chemical composition of the polymer and can result in a decrease in resistivity of the surface-near layer. Sheet resistances for irradiated PI films as low as 100  $\Omega$  have been reported [17]. These changes were connected to a carbonization of the substrate, i.e., an increase in the atomic percentage of carbon while functional groups are lost [17], [18]. With increasing

Ar ion current densities and fluences, an increase in carbonization and a further decrease of the substrate resistivity were observed. These results were mostly obtained at ion energies of several 10 to a few 100 keV. However, characteristic chemical changes in the XPS spectra during the decomposition of the PI structure have also been found at an ion energy of 500 eV – only slightly higher than the energy applied in this study [19]. Rutherford back-scattering scans revealed that the thickness of the modified layer is around 100 nm at an ion energy of 40 keV and current densities between 1 and 16  $\mu\text{A}/\text{cm}^2$  [18]. Most of the changes in the chemical composition of the polymer surface induced by IBE could be removed using a gas cluster ion beam (GCIB) [20].

These findings imply that even if IBE may completely remove the metallization on our polymer films as intended, the process can presumably result in a transformation of the substrate surface into a conductive material. Thus, the aim of the process development reported in this paper was, first, the complete etching of the sputter-deposited metal film and, second, the removal of a possible surface-near defect layer in the polymer substrate. A combination of different process parameters for IBE and the subsequent plasma etching (PE) step were tested in order to clarify whether the observed changes in resistance are due to (i) a modification of the substrate or (ii) a contamination of the surface with residual or redeposited metal, and (iii) whether cleaning of the substrate surface is possible by PE. For these tests, 5.5- $\mu\text{m}$ -thick PI layers were deposited on 4-inch wafers. Only one half of each wafer was then coated with a 200-nm-thick Pt film, in order to characterize the effectiveness of the etching steps and investigate metal redeposition during the etching processes. For the subsequent patterning process using IBE, the layers were coated with a photoresist mask. We varied the duration of the IBE step between 11 min 22 s and 20 min 28 s to adjust the Ar ion fluence on four substrates (samples S1 to S4). All other IBE parameters are as listed in Section II.B. At an etch rate of 22 nm/min, even the shortest etch duration is sufficient to etch through the Pt layer. The etching results were examined using optical microscopy and profilometry. Ion fluences were calculated from the etch duration during which only the polymer was exposed to the ion beam using the nominal ion current density of 0.822  $\text{mA}/\text{cm}^2$ . One substrate (sample S5) was post-processed by oxygen PE (PE parameters are given

**TABLE I**  
DESIGN PARAMETERS OF IDES FOR SHEET RESISTANCE MEASUREMENT

Finger pairs $n$	Interface length $L$ ( $\mu\text{m}$ )	Separation $s$ ( $\mu\text{m}$ )	Total length $n \times L$ (mm)	Number of squares $N$ ( $10^{-5}$ )
39	5500	15	214.5	7.0
29	"	"	159.5	9.4
19	"	"	104.5	14.4
9	"	"	49.5	30.3
7	"	"	38.5	39.0
5	"	"	27.5	54.5

in Sec. II.B) after patterning the Pt layer using the same IBE duration of 16 min 49 s as for sample S3. After the IBE and PE steps, the samples were cleaned in acetone, isopropanol, and deionized water supported by ultrasonic agitation. Sections of the PI substrates were then taken from samples S1-S5 for X-ray photoelectron spectroscopy (XPS). We examined the previously coated and uncoated wafer halves for changes of the substrate composition and possible Pt residues. Finally, the sheet resistances of all substrates were measured after etching and after coating and subsequent imidization of a second PI layer.

XPS measurements were performed using a K-Alpha+ XPS spectrometer (ThermoFisher Scientific, East Grinstead, UK). Data acquisition and processing using the Thermo Avantage software is described elsewhere [21]. All polyimide samples were analyzed using a microfocused, monochromated Al  $K\alpha$  X-ray source (spot size 400  $\mu\text{m}$ ). The K-Alpha+ charge compensation system was employed during material analysis, using electrons with an energy of 8 eV and low-energy Ar ions to prevent any localized charge build-up. The spectra were fitted with one or more Voigt profiles (binding energy uncertainty:  $\pm 0.2$  eV); Scofield sensitivity factors were applied for quantification [22]. All spectra were referenced to the C1s peak (C-C, C-H) at a binding energy (BE) of 285.0 eV controlled by means of the well-known photoelectron peaks of metallic Cu, Ag, and Au, respectively.

For the electrical characterization of the PI substrates after ion irradiation, we implemented interdigitated electrodes (IDEs) in the Pt layer during the IBE step to determine the sheet resistance of the substrate. We recorded the electrical resistance between the fingers of the IDEs as a function of process parameters, processing steps and time. The recorded resistances  $R$ , the number of IDE finger pairs  $n$ , the finger length  $L$ , and separation distance  $s$  are related to the sheet resistance  $R_{\text{sq}}$  via

$$R_{\text{sq}} = R n L/s = R/N.$$

Note that  $L/s$  denotes the inverse of the effective number of squares separating a pair of fingers, since  $s$  denotes the length of the conductive region between the pair and  $L$  is the width of that region. The term  $n$  in the numerator takes into account the parallel conduction by  $n$  such pairs. Overall  $nL/s = 1/N$  is the effective number of squares between all pairs of fingers of an IDE. Design parameters of the characterized IDEs are listed in Table I. For comparison to our neural probes, the parameter  $N$  of a 30-mm-long PI cable is  $36.0 \times 10^{-5}$ .

The resistance measurements were performed with the PI films still adhering to the Si substrates using a shielded setup with triaxial measurement lines connected to an electrometer (Keithley Model 6514, Tektronix UK Ltd., Berkshire, UK) with a measurement range up to 200 G $\Omega$ . Between electrical measurements, the samples were stored in air at an ambient temperature of  $21.8 \pm 0.3$  °C and a relative humidity of  $33 \pm 5$  % rH.

#### D. Probe Stiffening and Insertion Experiment

The insertion shuttles for implantation of the flexible probes are custom-made from Si. We applied a similar fabrication procedure as for the probe tips and consequently patterned the Si substrates using the EBG process. For the stiffening procedure, a flexible probe is placed on a fluoropolymer foil covering a hotplate set to 40 °C {Fig. 3(a&b)}. Then, the shuttle is slit onto the probe until the two components connect at the flat end of the probe tip. The shuttle design leaves a 5- $\mu\text{m}$ -wide lateral gap between sides of the probe tip and the shuttle. The gap ensures the reliable probe release after implantation. Using a wire loop heated to 80 °C, the gaps between probe and shuttle are filled with molten PEG-1500, which acts as a water-soluble adhesive bond between the components. During this procedure, surface tension keeps the PEG drop on the wire loop while capillary forces drive the liquid into the gaps of the assembly. Finally, the stiffened probe is placed on a precision-machined aluminum inserter for implantation {Fig. 3(c,d)}. The inserter connects the shuttle to a linear motor (Physik Instrumente GmbH & Co. KG, Karlsruhe, Germany) and aligns the shuttle parallel to the implantation direction by dowel pins fitting to the notches implemented in the shuttle.

The implantation experiments were performed using a brain model composed of agar gel with a concentration of 0.6-wt% covered by two layers of a 10- $\mu\text{m}$ -thick polyethylene membrane mimicking the dura mater. The gel and membrane have been reported to exhibit mechanical properties comparable to those of grey matter and dura mater, respectively [23], [24]. Probes were descended into the brain model at a constant speed of 100  $\mu\text{m}/\text{s}$  to depths of around to 7.5 mm. The reaction forces were recorded below the brain model using a miniature load cell (Model 31 Low, Honeywell International Inc, Golden Valley, MN, USA) connected to a nanovoltmeter (Keysight 34420A, Keysight Technologies Deutschland GmbH, Boeblingen, Germany). For control and readout of the setup, we implemented a LabVIEW program. The whole procedure was optically inspected using a USB microscope camera.

## III. RESULTS AND DISCUSSION

#### A. Neural Probes

Exemplary fabrication results for the passive and the CMOS-based, active, flexible neural probes are shown in Figs. 4 and 5, respectively. Fig. 4(a) shows a conventional Michigan-style probe of our lab alongside our new, hybrid neural probe. Both devices are passive and feature 32 channels. The new probe, however, exhibits a strongly increased feature density with the

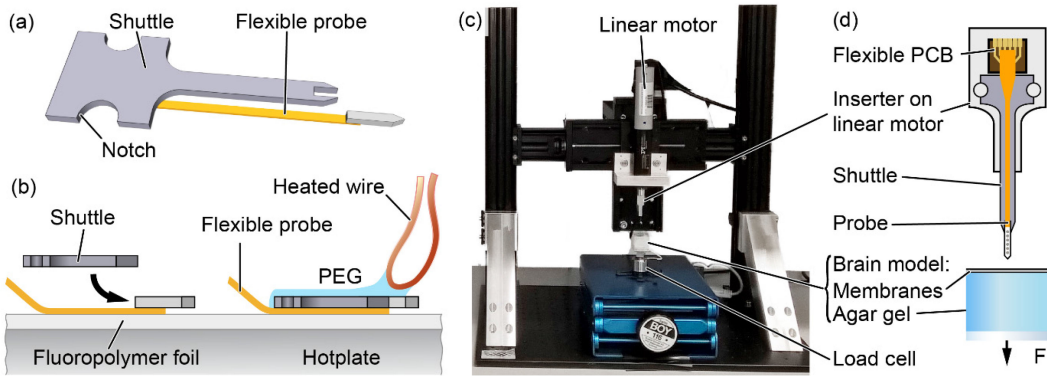


**Fig. 3.** (a) 3D model of shuttle and probe, (b) schematic of stiffening procedure, and (c) photograph providing an overview of the insertion setup (USB microscope not shown for clarity). (d) Schematic representation of insertion setup and details of the inserter with the stiffened neural probe.

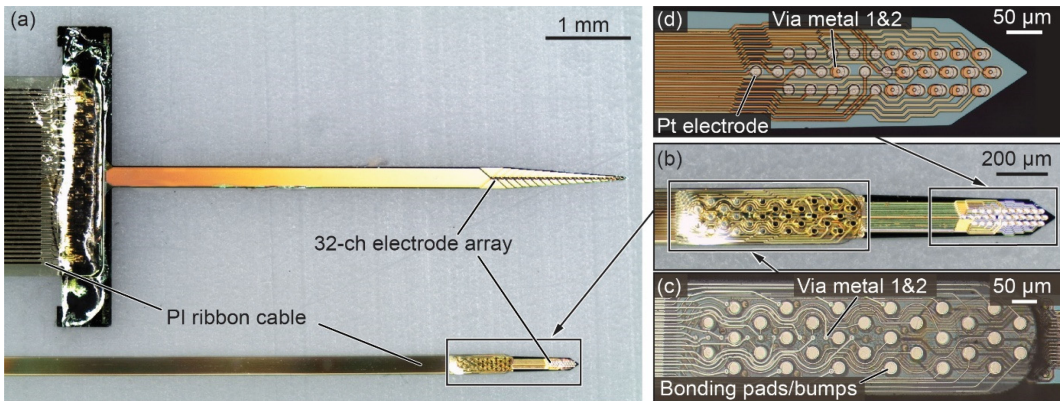


**Fig. 4.** Micrographs of (a) (top) conventional and (bottom) flexible Si-based neural probes and details of (b) probe tip region, (c) bond interface and (d) electrode array.

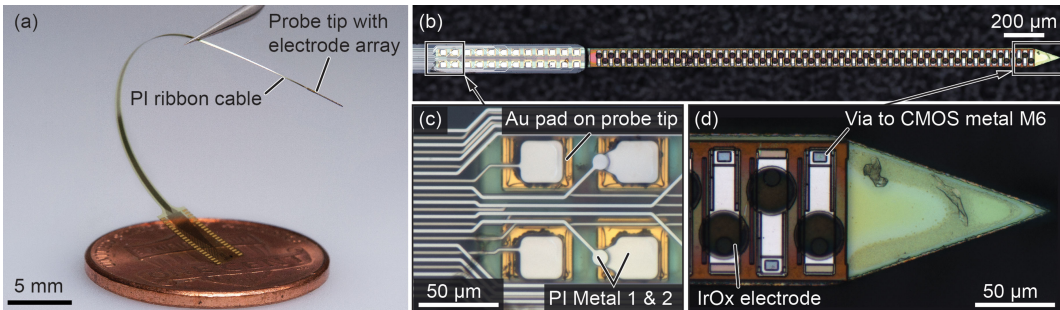


**Fig. 5.** (a) Photograph of the active, flexible neural probe with 72  $\text{IrO}_x$  recording sites; optical micrographs show (b) the complete probe tip region, (c) part of the densely packed interface region and (d) tip of the probe with three electrode blocks comprising integrated circuitry.

interface region {Fig. 4(b,c)} and electrode array {Fig. 4(d)} integrated in the 1.3-mm-long probe tip. The electrode array consists of Pt electrodes with a diameter of 15  $\mu\text{m}$ . The electrical impedance of the electrodes measured in 1 M Ringer's solution was determined to be 1.44  $\text{M}\Omega$  at 1 kHz, with only the electrodes immersed in the electrolyte. After immersion of the complete probe tip and a 6-mm-long section of the cable, the magnitude of the impedance dropped by less than 1% for frequencies around 1 kHz while the phase decreased to a similar extent. The effect increased with increasing frequencies to around 5% for frequencies above 100 kHz. We interpret this as a minor increase in the capacitive coupling to the surrounding electrolyte. However, the

impact is small, and none of the recorded channels showed a severe drop of the electrode impedance that might have been caused by a short circuit due to pinholes or a leakage at the bond interface.

Fig. 5 shows an active probe with 24 input/output channels and 72  $\text{IrO}_x$  electrode sites. The tip of this probe is 3.1 mm long and contains the interface region, electronics and electrode array {Fig. 5(b)}. Details of the highly dense interface region and the tip region with three of the individually addressable electrode blocks are shown in Figs. 5(c) and (d), respectively. A detailed demonstration of the function of CMOS electrode array has been presented earlier [8].

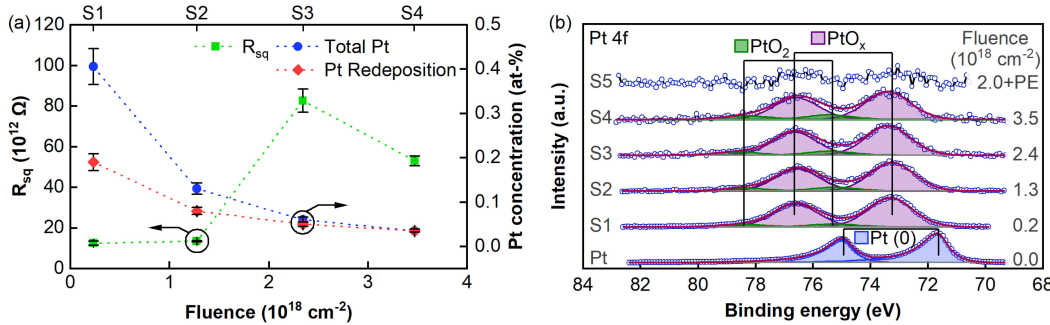


Fig. 6. (a)  $R_{sq}$  and Pt concentration as a function of increasing Ar ion fluence on samples S1 to S4 after IBE and (b) X-ray photoelectron spectra of Pt4f peaks before and after patterning on samples S1 to S5. All spectra are normalized to the maximum of intensity.

Figs. 4(c) and 5(c) also demonstrate the high quality of our pattern transfer for the Pt-based metallization layers in the PI cables with line widths and spacings as low as 2 and 3  $\mu\text{m}$ , respectively. Based on our observations, we recommend that wet chemical stripping of the photoresist mask after Pt etching is performed carefully and in combination microoptical inspection, as the resist hardens during ion milling and exhibits a reduced solubility in acetone. Fortunately, the chemical attack of the PE step on the hardened surface of the photoresist mask strongly aids in stripping of the resist.

### B. Sheet Resistance and XPS Analysis of PI Substrates after IBE and PE

**1) IBE Duration and Post-Processing by PE:** All process parameters tested in the IBE step resulted apparently in clean, metal-free substrate surfaces with a good reproduction of patterns in the remaining, masked Pt layer. From the profilometer measurements and optical inspection, it was certain that the Pt layers on all samples were completely etched through. With increasing IBE duration, the etch depths in the PI substrate increased from around 30 nm on sample S1 to around 440 nm on sample S4. Electrical testing, however, revealed a lowered sheet resistance for all samples that were solely processed by IBE. Fig. 6(a) shows the extracted  $R_{sq}$  of Samples S1 to S4 as a function of ion fluence received by the PI substrate (fitting of  $R_{sq}$  with  $R^2 > 0.985$ ; error bars for  $R_{sq}$  in Fig. 6(a) indicate the standard deviation). The resistance of these samples is still very high, especially compared to other samples in this study and earlier experiments, but it is significantly lowered compared to pristine PI (pristine PI exhibits a surface resistivity  $> 10^{16} \Omega$  and volume resistivity  $> 10^{16} \Omega\text{cm}$ , as given by the manufacturer [25]). We found that the  $R_{sq}$  of the IBE-samples does not show a clear trend with fluence. After a small increase of  $R_{sq}$  with ion fluence from samples S1 to S2, it rises strongly for sample S3. At the highest etching duration, however, the sheet resistance drops again significantly.

The XPS analysis of the Pt4f peak as a function of ion fluence showed small traces of Pt on all four samples {Fig. 6(a)}; all concentrations with an uncertainty of 10%. However, in contrast to the behavior of  $R_{sq}$ , the Pt concentration on the surface decreased monotonously with prolonged etching. Obviously, the  $R_{sq}$  and the Pt contamination levels are not correlated.

Furthermore, it seems clear that IBE is unsuitable for a complete removal of the metallization as the Pt concentration only decreases asymptotically in this IBE parameter range {Fig. 6(a)}. This is likely due to the fact that the contamination of the surfaces is only in part due to residues of the initial Pt film. The Pt concentration found on the initially metal-free wafer halves must result from Pt redeposition and makes up for at least 50% of the total metal concentration found on the individual samples {Fig. 6(a)}. Metal redeposition is clearly the reason for persistent Pt levels at high fluences.

The deconvolution of the Pt 4f peaks before and after IBE revealed a significant chemical shift after irradiation already at the lowest ion fluence of  $2 \times 10^{17} \text{ cm}^{-2}$  in case of sample S1 {Fig. 6(b)}. The Pt 4f doublet of the as-deposited Pt layer shows the typical asymmetric peak shape of metallic Pt, and the Pt4f<sub>7/2</sub> level appears at a BE of 71.6 eV. After irradiation, two symmetric doublets can be found in the spectra, one with Pt4f<sub>7/2</sub> at a BE of 73.4 eV (PtO<sub>x</sub>) and the other at 75.4 eV (PtO<sub>2</sub>). The contribution of the higher order oxide increases slightly with fluence. The pronounced chemical shift clearly shows that the Pt contamination in the irradiated films is not in the metallic form, but rather seems to be oxidized within a depth of at least 10 nm. From this analysis, it is, however, unclear whether the oxidized Pt has interacted with the organic compounds in the film, as has been proposed for implanted tungsten ions [26], or whether the Pt compounds are participating in the electrical conduction of the surface layer.

The applied PE step proved to be more effective in cleaning the PI surface than IBE. On the surface of the PE-treated sample S5, no Pt contamination was found {Fig. 6(b)}. The total etch depth in the PI substrate of sample S5 was determined to be only 350 nm; roughly 100 nm less than for the longest IBE duration. The PE step accounts for around 110 nm of this total etch depth, which is expected to be sufficient to remove a possible, surface-near defect layer introduced by IBE [18]. After the PE processing step, all IDE resistances exceeded the measurement range of our setup, indicating a sheet resistance higher than  $2.9 \times 10^{15} \Omega$ .

The XPS analysis of the C1s, N1s, and O1s spectra for samples S1 to S5 revealed that, indeed, IBE strongly altered the composition of the PI substrate (Fig. 7). In contrast to studies performed at higher ion energies, we did not find a shift in the elemental ratios of carbon and nitrogen or oxygen that would

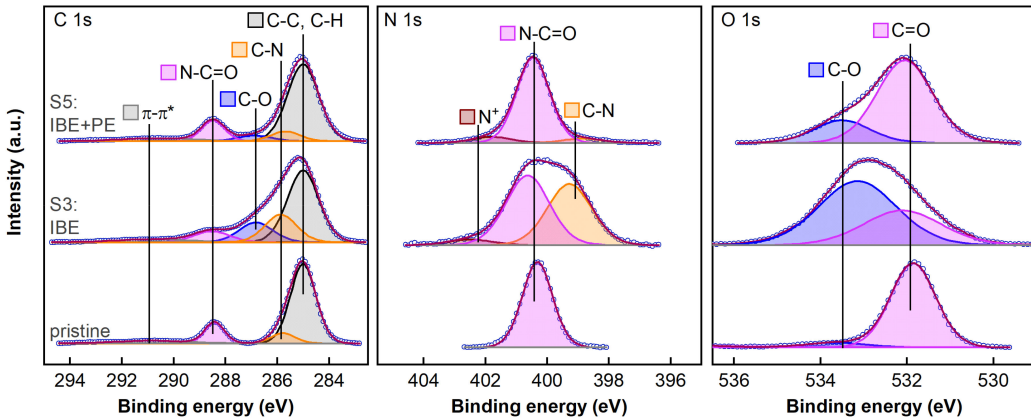


**Fig. 7.** C1s, N1s, and O1s X-ray photoelectron spectra of PI films after PI coating (pristine), IBE (S3) and IBE+PE (S5).

point towards a carbonization of the substrate. However, the changes in the composition of the individual peaks are similar to those documented for the decomposition of PI [19], [27]. Especially the increase in intensity and the additional components in the spectra of C1s at BEs of 285.8 eV (C-N) and 286.9 eV (C-O), N1s at a BE of 399.1 eV (C-N) and O1s at a BE of 533.3 eV (C-O) are characteristic for the decomposition of the PI structure. This happens mostly at the cost of the imide groups. The changes in the composition of sample S3 were observed for all IBE-samples. As shown in Fig. 7, our PE post-process effectively removes the damaged PI layer and permits the recovery of a surface very similar to the pristine one, with only a slight remaining oxidation of the substrate surface (C-O).

Based on these results, it seems likely that the decrease in  $R_{sq}$  after IBE is a result of the decomposition of the polymer substrate. The similar degree of decomposition for all IBE-samples found in the XPS analysis would explain the lack of a trend of the  $R_{sq}$  with fluence. The variation of the  $R_{sq}$  observed for samples S1-S4 is likely due to the nature of this process. Strong, random variations of  $R_{sq}$  for some fluences and current densities have also been found in other studies [17], [18]. The significant drop in Pt concentration from sample S1 to sample S2 and the almost constant  $R_{sq}$  of these samples further supports the hypothesis that the decrease in  $R_{sq}$  is due to the polymer decomposition rather than metal residues. Also, another sample processed with the same parameters as sample S3 (fluence of  $2.3 \times 10^{18} \text{ cm}^{-2}$ ), exhibited a similar Pt concentration of less than 0.1 at-% Pt, but a significantly lower  $R_{sq}$  of  $1.7 \times 10^{12} \Omega$ . The restored, high resistance of the PI substrate after PE can be explained by the near-pristine composition of the surface-near layers after this etching step.

**2) Aging and Stability of PI Films After IBE and PE:** Fig. 8 shows the sheet resistance of a sample (S6) processed by IBE with the same parameters as used for samples S3 and S5, where the Pt layer is over-etched by around 150 nm. The resistance was measured over a period of 140 days. The initial sheet resistance ( $R_{sq,0}$ ) was only  $2.7 \times 10^6 \Omega$ . The resulting shunt resistance for our implants at such a low  $R_{sq}$  value would be around 1 k $\Omega$ . Over time, the resistance increased exponentially as  $R_{sq}(t) = R_{sq,0} \times \exp(t/\tau)$  with an initial rate of  $1/\tau = 1.38 \times 10^{-6} \text{ s}^{-1}$ , which decreased later to  $1/\tau = 0.27 \times 10^{-6} \text{ s}^{-1}$ . The sheet resistance  $R_{sq}$

reached a value of around  $7 \times 10^8 \Omega$  at day 140. When stored for aging, samples S1 to S4 showed a similar increase in resistance over a duration of 42 days ( $1/\tau = 0.76 \times 10^{-6} \text{ s}^{-1}$  on average), as shown in Fig. 8(b). After coating a second PI layer on day 42, the  $R_{sq}$  dropped by a factor of around  $5 \times 10^{-5}$  to critically low values. The equivalent shunt resistance for a 30-mm-long cable would be 1 M $\Omega$ . After the PI coating step, the sheet resistances kept increasing, however at a higher average rate of  $1/\tau = 2.12 \times 10^{-6} \text{ s}^{-1}$ .

The resistance increase over time points towards effects taking place in the irradiated polymer. It has been shown for plasma treated polymer surfaces that the water contact angle features a dynamic behavior over time. This was associated with the migration of functional groups in the damaged polymer [28]. It seems plausible that such a mechanism also affects the electrical conduction in the modified polymer surface. We assume that the drop in resistance after imidization of the second PI layer is also due to an interaction between the defect layer and the PI precursor. Clearly, layers prepared only by IBE are unstable for further processing and fabrication of PI cables. In contrast, the IDE resistances of the PE-treated sample S5 did not drop to a measurable range after coating with a second PI layer.

The XPS analysis of samples S3 and S5 after aging in air for one month, revealed significant intensity shifts in the O1s peak of sample S3 (Fig. 9). The most notable changes were found as an increase of the peak at a BE of 532.0 eV (C = O) and a decrease of that at 533.3 eV (C-O). The decrease in intensity of IBE-induced C-O peak might be linked to the recovery of the  $R_{sq}$  of the material. The C1s peak of sample S3 showed inconsistent fluctuations depending on the probing region (data not shown). In contrast, the XPS spectra of sample S5 showed no notable signs of aging and demonstrate the stability of this PE-treated surface for durations of 1 month (Fig. 9).

Our data support the hypothesis that the surface-near defect layer resulting from IBE creates instable species on the film surfaces, which likely affect the electrical properties of the samples. As there are no shifts in the Pt 4f peak of sample S3 after aging, it seems safe to link the changes in  $R_{sq}$  only to changes in the organic species. In summary, our analyses showed that films prepared with IBE in combination with PE are electrically and chemically stable.

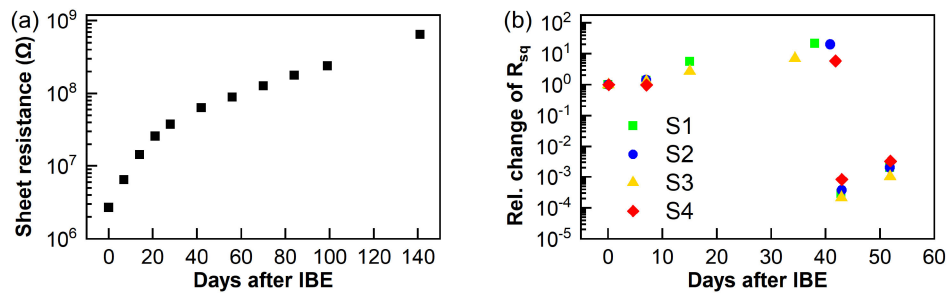


**Fig. 8.** XPS data of sample S3 and PE-Sample S5 after the etching processes and after aging in air for one month. All peaks were fitted as in Fig. 7.

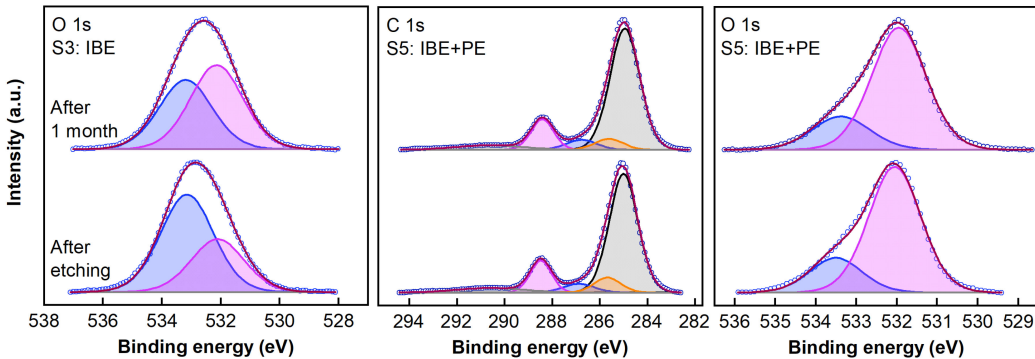


**Fig. 9.** Micrographs of a stiffened 120- $\mu\text{m}$ -wide probe; (a) overview, close-up of tip region from (b) front and (c) rear.

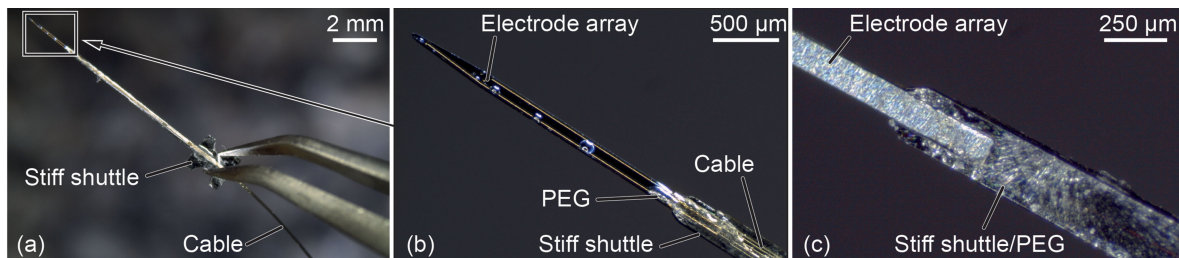


**Fig. 10.** (a) Sheet resistance of sample S6 measured over a period of 140 days after IBE. (b) Relative change of sheet resistance of samples S1 to S4 over 60 days after IBE. After 42 days, samples were coated with a second PI layer.

### C. Probe Implantation

Fig. 10 shows a flexible probe bonded to an insertion shuttle for the implantation experiments. Small amounts of excess PEG were found in some cases on the probe tip and on the side of the shuttle that is facing down during coating. The unwanted PEG structures are in general less than  $15 \mu\text{m}$  in thickness and can be washed away by shortly dipping the probe into DI water prior to its use. The mounting procedure results in well-aligned assemblies with a flush transition from shuttle to the Si-based electrode array at the tip of the probe {Fig. 10(c)}. In comparison to our previous approach with molded PEG insertion vehicles [12], the novel shuttles exhibit a smaller cross-section and can accept higher buckling forces. Further, one has better control over the mechanical properties of the shuttles and can adapt their lateral as well as vertical dimensions to the probe tips more freely and with higher resolution.

We inserted 18 probes orthogonally into the agar-based brain model covered with polyethylene membranes at a speed of

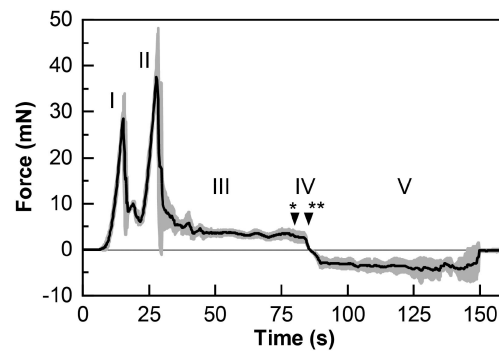


**Fig. 11.** Mean and standard deviation of force recorded during probe implantation into brain model for five probes with cross-section of  $120 \times 50 \mu\text{m}^2$  to a depth of around 7.5 mm at an insertion speed of  $100 \mu\text{m}/\text{s}$ . \*End of insertion \*\*Start of retraction.

$100 \mu\text{m}/\text{s}$ . The probes withstood axial forces of at least 63 mN. Generally, the magnitude of the recorded forces was in good

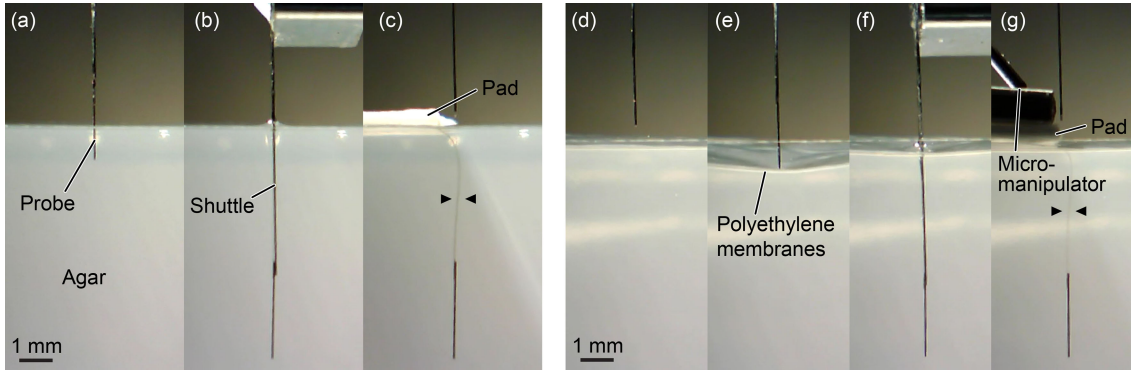


**Fig. 12.** Micrographs of the implantation of stiffened probes into (a–c) agar gel and (d–g) brain model with PE membrane. Probes are shown in side-view. Triangular markers highlight the position of the PI cable. Retraction of the insertion shuttle has no obvious effect on the position of the probe tip.

agreement with *in vitro* and *in vivo* data [24]. The mean force profile and its standard deviation for five probes with identical tip shape, length and cross-section of  $120 \times 50 \mu\text{m}^2$  is shown exemplarily in Fig. 11. Differences in the probe shape did not critically affect the insertion behavior or the characteristic force profile, although there are minor variations in the height and location of main features. The peaks I and II result from the probe tip and the wider inserter, respectively. After puncturing the membrane, an offset force of  $3.2 \pm 0.6 \text{ mN}$  results from the interaction between the polyethylene membranes and the shuttle (region III). Such a force has also been recorded in *in vivo* experiments when implanting Si probes through the intact rat pia/dura mater [24]. Even after the forward movement ended in our experiment (\* in Fig. 11), a remanent force was recorded. Upon retraction of the inserter (starting at \*\* in Fig. 11), the offset force was also reversed and stayed at around  $-2.7 \pm 1.3 \text{ mN}$ .

The static force in region IV affected to a certain extent the probe deployment. Without polyethylene membranes covering the agar-gel, the implantation of shuttle-stiffened probes into agar gel succeeded without any difficulty {Fig. 12(a–c)}. In order to keep the probe at its intended implantation depth, it is necessary to remove the PCB at the end of the PI cable from the inserter tool and secure it, before dissolving the PEG bond between probe and shuttle by rinsing with water. This has already been shown for a similar approach [29]. In addition to this procedure, we secured the cable on the surface of the brain model with a pad that also absorbed the water meniscus that otherwise forms between cable and shuttle and is likely to pull on the cable during explantation. If cable and shuttle are separated while immersed in a liquid, e.g., cerebrospinal fluid, no meniscus can form between the components and the pad is not required.

The PEG bond between the implanted portion of probe and shuttle starts to dissolve directly after implantation. Five minutes after implantation, we could retract the inserter tool at speeds between 50 and  $200 \mu\text{m/s}$ . Placing the probe at its target location using this method was successful and the final position was unaffected by the retraction step.

Reference [29] discusses the use of a specific explantation protocol to improve the accuracy of the probe deployment in agar gel. This protocol involves a high-speed movement im-

pulse over a short distance to break static friction between cable and shuttle. In our experiments in gel, we did not observe significant shifts of the probe tip during retraction of the shuttle even for the slowest explantation speed of  $50 \mu\text{m/s}$ . After dissolution of the PEG, the interaction between shuttle and probe should originate from the viscosity of the water film between the two components. A slower movement of the shuttle should thus result in lower shear forces acting on the cable, which consequently will minimize probe displacement.

For the brain model with PE membranes, the retraction protocol had to be adapted {Fig. 12(d–g)}. When we simply retracted the shuttle in the last step, the cable was randomly pulled upwards. Likely, the remanent force recorded in region IV in Fig. 11 compressed the gap between shuttle and cable at the entry point into the brain phantom. This resulted in friction forces between shuttle and cable and displaced the probe. We used a micromanipulator to improve the fixation of the cable at the surface of the brain model {Fig. 12(g)}. The micromanipulator was descended until it made contact with the absorber pad placed on the cable. During extraction, the manipulator inhibited the upwards deflection of the polyethylene membrane and helped to shear off the cable from the shuttle. The method proved successful with no observable shift of the probe tip.

As the remanent force acting on an implanted probe is present *in vivo*, we expect the compression of probe/shuttle assemblies to also be present *in vivo*. This renders the use of appropriate countermeasures against probe displacement, such as the probe fixation with the micromanipulator, relevant for shuttles-based probe delivery concepts in general. Even though our results support the applicability of this concept for probe implantation through dura, likely it is advantageous to form a small incision in the meninges at the implantation site to eliminate the forces restricting the probe release. Furthermore, opening the dura prior to implantation would reduce the blunt trauma from puncturing the meninges with the probe. The subsequent probe deployment would work safely as demonstrated in the brain models without polyethylene membranes.

It has to be noted that the fast dissolution of PEG in combination with the intended, limited geometrical overlap between shuttle and probe tip bears the risk of a deflection of the probe during implantation. While critical deflections were not observed in our experiments, selecting an adhesive with

slower dissolution rate will increase the stability of the assembly during insertion and reduce the likelihood of probe deflection.

#### IV. CONCLUSION

We presented an improved technology for the fabrication and implantation of ultra-compact, flexible, CMOS-compatible neural probes. The flexibility of these probes and their small size will likely alleviate the FBR common with Si-based probes. In addition to the improved mechanical and geometrical properties, our active probes offer highly dense electrode arrays that, in combination with EDC [13], allow to actively improve signal yield.

For the fabrication of up to 30-mm-long PI cables, we developed a reliable, high-resolution patterning process for Pt films using Ar IBE and oxygen PE. We found that the reduction and instability of the sheet resistance  $R_{sq}$  after IBE is most likely related to chemical changes in the polymer and not to residual Pt. Post-processing of the substrate after IBE using PE resulted in polymer surfaces of near-pristine composition that exhibit stable chemical and electrical properties.

The implantation of the hybrid probes was accomplished with Si-based stiff insertion shuttles. In agar gels, probe insertion at 100  $\mu\text{m/s}$  and detachment from the shuttle is simple and reliable. With polyethylene membranes mimicking the brain meninges, we showed that our probes withstand typical *in vivo* implantation forces. Our insertion force measurement supports the hypothesis that the direct probe detachment is hindered by the compression of the shuttle/probe assembly by the membranes. This situation and appropriate countermeasures have to be considered when using insertion shuttles in *in vivo* experiments. Our method of fixating the PI cable using a micromanipulator allowed us to successfully place the flexible probes in the model tissue even in the presence of the compressive force.

Future experiments have to focus on the long-term stability of the probe components and recording functionality. This should be evaluated in comparison to rigid Michigan-style probes in an appropriate animal model.

#### ACKNOWLEDGMENT

The authors would like to thank A. Sayed-Herbawi for providing CMOS-based EDC probes developed with funding from BrainLinks-BrainTools.

#### REFERENCES

- [1] H. Xu *et al.*, "Acute *in vivo* testing of a conformal polymer microelectrode array for multi-region hippocampal recordings," *J. Neural Eng.*, vol. 15, no. 1, 2018, Art. no. 016017.
- [2] S. Sommakkia *et al.*, "Materials approaches for modulating neural tissue responses to implanted microelectrodes through mechanical and biochemical means," *Current Opin. Solid State Mater. Sci.*, vol. 18, no. 6, pp. 1366–1376, Dec. 2014.
- [3] I. H. Stevenson and K. P. Kording, "How advances in neural recording affect data analysis," *Nature Neurosci.*, vol. 14, no. 2, pp. 139–42, Feb. 2011.
- [4] P. Ruther and O. Paul, "New approaches for CMOS-based devices for large-scale neural recording," *Current Opin. Neurobiol.*, vol. 32, pp. 31–37, 2015.
- [5] B. C. Raducanu *et al.*, "Time multiplexed active neural probe with 1356 parallel recording sites," *Sensors*, vol. 17, no. 10, Oct. 2017, Art. no. E2388.
- [6] J. L. Skousen *et al.*, "Reducing surface area while maintaining implant penetrating profile lowers the brain foreign body response to chronically implanted planar silicon microelectrode arrays," *Prog. Brain Res.*, vol. 194, pp. 167–80, Jan. 2011.
- [7] J. Thelin *et al.*, "Implant size and fixation mode strongly influence tissue reactions in the CNS," *PloS One*, vol. 6, no. 1, Jan. 2011, Art. no. e16267.
- [8] A. S. Herbawi *et al.*, "CMOS-based neural probe with enhanced electronic depth control," in *Proc. 18th Int. Conf. Solid-State Sens. Actuators Microsyst.*, 2015, pp. 1723–1726.
- [9] R. Biran, D. C. Martin, and P. A. Tresco, "The brain tissue response to implanted silicon microelectrode arrays is increased when the device is tethered to the skull," *J. Biomed. Mater. Res. A*, vol. 82, no. 1, pp. 169–178, Jul. 2007.
- [10] A. Schander *et al.*, "Silicon-based microfabrication of free-floating neural probes and insertion tool for chronic applications," *Micromachines*, vol. 9, no. 3, 2018, Art. no. 131.
- [11] J. Subbarayan, D. C. Martin, and D. R. Kipke, "A finite-element model of the mechanical effects of implantable microelectrodes in the cerebral cortex," *J. Neural Eng.*, vol. 2, no. 4, pp. 103–113, 2005.
- [12] F. Barz *et al.*, "Flexible silicon-polymer neural probe rigidified by dissolvable insertion vehicle for high-resolution neural recording with improved duration," in *Proc. IEEE 28th Int. Conf. Micro Electro Mech. Syst.*, 2015, pp. 636–639.
- [13] K. Seidl *et al.*, "CMOS-based high-density silicon microprobe array for electronic depth control in neural recording," in *Proc. 22nd Int. Conf. Micro Electro Mech. Syst.*, 2009, pp. 232–235.
- [14] S. Herwik, O. Paul, and P. Ruther, "Ultrathin silicon chips of arbitrary shape by etching before grinding," *J. Microelectromech. Syst.*, vol. 20, no. 4, pp. 791–793, Aug. 2011.
- [15] S. Kisban *et al.*, "Microprobe array with low impedance electrodes and highly flexible polyimide cables for acute neural recording," in *Proc. 29th Annu. Int. Conf. IEEE Eng. Med. Biol. Soc.*, vol. 2007, pp. 175–178, Jan. 2007.
- [16] S. Kisban *et al.*, "A novel assembly method for silicon-based neural devices," in *Proc. IFMBE*, 2009, pp. 107–110.
- [17] M. Iwaki, "Ion surface treatments on organic materials," *Nucl. Instrum. Methods Phys. Res. Sec. B, Beam Interact. Mater. Atoms*, vol. 175–177, pp. 368–374, 2001.
- [18] V. N. Popok *et al.*, "Radiation-induced change of polyimide properties under high-fluence and high ion current density implantation," *Appl. Phys. Mater. Sci. Process.*, vol. 78, no. 7, pp. 1067–1072, Apr. 2004.
- [19] A. M. Ektessabi and S. Hakamata, "XPS study of ion beam modified polyimide films," *Thin Solid Films*, vol. 377–378, 2000, pp. 621–625.
- [20] T. Miyakawa *et al.*, "Removal of Ar+ beam-induced damaged layers from polyimide surfaces with argon gas cluster ion beams," *Surf. Interface Anal.*, vol. 42, no. 9, pp. 1453–1457, 2010.
- [21] K. L. Parry *et al.*, "ARXPS characterisation of plasma polymerised surface chemical gradients," *Surf. Interface Anal.*, vol. 38, no. 11, pp. 1497–1504, Nov. 2006.
- [22] J. H. Scofield, "Hartree–Slater subshell photoionization cross-sections at 1254 and 1487 eV," *J. Electron Spectrosc. Related Phenomena*, vol. 8, no. 2, pp. 129–137, 1976.
- [23] S. Snow, S. C. Jacobsen, D. L. Wells, and K. W. Horch, "Microfabricated cylindrical multielectrodes for neural stimulation," *IEEE Trans. Biomed. Eng.*, vol. 53, no. 2, pp. 320–326, Feb. 2006.
- [24] N. H. Hosseini, R. Hoffmann, S. Kisban, T. Stieglitz, O. Paul, and P. Ruther, "Comparative study on the insertion behavior of cerebral microprobes," in *Proc. 29th Annu. Int. Conf. IEEE Eng. Med. Biol. Soc.*, vol. 2007, Jan. 2007, pp. 4711–4714.
- [25] Ltd. Ube Industries, "Characteristics of UPIA." [Online]. Available: [http://www.upilex.jp/en/varnish\\_grade.html#01](http://www.upilex.jp/en/varnish_grade.html#01). Accessed: Mar. 21, 2018.
- [26] M. Iwaki *et al.*, "Characterization of Ag- and W-implanted polyimide films," *Nucl. Inst. Methods Phys. Res. B*, vol. 80–81, no. PART 2, pp. 1080–1084, 1993.
- [27] K. Sahre *et al.*, "Characterization of ion-beam modified polyimide layers," *Surf. Coat. Technol.*, vol. 139, no. 2/3, pp. 257–264, 2001.
- [28] T. Murakami, S. Kuroda, and Z. Osawa, "Dynamics of polymeric solid surfaces treated with oxygen plasma: Effect of aging media after plasma treatment," *J. Colloid Interface Sci.*, vol. 202, no. 1, pp. 37–44, 1998.
- [29] S. H. Felix *et al.*, "Insertion of flexible neural probes using rigid stiffeners attached with biodissolvable adhesive," *J. Vis. Exp.*, no. 79, pp. 1–12, 2013.